

36 method, RMSE decreases by $39.95 \mu\text{g}/\text{m}^3$, and the relative deviation reduces by 44.87%.
37 Moreover, validation at two AERONET sites presents a time series change closer to the
38 true values, with an R of about 0.80. This study is also a preliminary attempt to combine
39 model-driven and data-driven models, laying a foundation for further atmospheric
40 research on optimization methods.

41 **Keywords:** PM_{2.5}; Physical approach; Machine learning; Volume-to-extinction ratio;
42 Fine mode fraction

43

44 **1. Introduction**

45 Epidemiological studies have indicated that PM_{2.5} (fine particulate matter with an
46 aerodynamic equivalent diameter no greater than $2.5 \mu\text{m}$) can adversely affect human
47 health, such as increasing the risk of diabetes and respiratory diseases (Bowe et al.,
48 2018; Pope III et al., 2002; Xu et al., 2013), and accurate surface PM_{2.5} concentration
49 is the basis of air pollution-health related research. Satellite remote sensing has the
50 advantages of high resolution and global coverage (Ma et al., 2014; Wu et al., 2020; He
51 et al., 2022), including variables strongly associated with PM_{2.5} such as aerosol optical
52 depth (AOD). Therefore, it has become a mainstream method for fine particle
53 estimation (Zhang et al., 2021).

54 There are mainly three satellite-based ways of retrieving PM_{2.5}. 1) Chemical transport
55 models-based method. It calculates a scaling factor η between AOD and PM_{2.5}
56 simulated by atmospheric chemical transport models (CTM) (Lyu et al., 2022; Xiao et
57 al., 2022) and then transfers the proportional relationship to satellite AOD data when
58 calculating surface PM_{2.5} concentration (Geng et al., 2015; Van Donkelaar et al., 2006).
59 However, the assumption of a constant factor between simulated and observed values
60 has large spatiotemporal limitations. 2) Univariate/Multivariate regression. This kind
61 of data-driven method establishes a statistical model between AOD, auxiliary variables,
62 and ground PM_{2.5} observations. Machine learning is a common tool for such regression
63 methods due to its powerful nonlinear fitting ability between multiple variables (Irrgang
64 et al., 2021). But the regression algorithms in machine learning are affected by the
65 distribution and density of ground stations (Gupta and Christopher, 2009; Li et al.,

66 2017). 3) Semi-empirical physical approach. Taking the physical theory as the basis,
67 surface $PM_{2.5}$ is derived through an empirical formula constructed from AOD and some
68 PM-related key parameters, including an important empirical parameter related to the
69 optical properties (S). The process steps are explicit and independent of ground station
70 observations. Meanwhile, this approach has stronger physical interpretability than the
71 previous two methods with a large space for optimization.

72 Due to the complexity of the physical parameters, many studies have optimized the
73 semi-empirical physical approach. Based on 355nm-band radar observations, Raut and
74 Chazette (2009) introduced a specific extinction cross-section to simplify the
75 expression of S and $PM_{2.5}$ concentration was estimated. Kokhanovsky et al. (2009)
76 constructed a particle-effective radius model, which can obtain the particle
77 concentrations throughout the atmospheric column. Furthermore, Zhang and Li (2015)
78 proposed the physical $PM_{2.5}$ remote sensing method (PMRS). It replaced S by defining
79 a volume-to-extinction ratio of fine particles (VE_f) and used a quadratic polynomial of
80 fine mode fraction (FMF) to simulate VE_f , showing certain advantages (Li et al., 2016;
81 Zhang et al., 2020).

82 However, the above semi-physical empirical models have some shortcomings. Firstly,
83 the satellite data used in the models are blocked by clouds and fog in some areas, thus
84 high-coverage and high-precision products need to be excavated and applied; secondly,
85 there are still large uncertainties in estimating physical parameters (such as a simple
86 polynomial fit to S in the PMRS method) and their expressions need to be improved.
87 To date, machine learning (ML) has developed rapidly (He et al., 2021). It can detect
88 complex nonlinear relationships of multiple data and model their interaction (Yuan et
89 al., 2020; Lee et al., 2022). This provides an idea for improving the accuracy of physical
90 parameter acquisition, so as to estimate high-precision $PM_{2.5}$ through semi-physical
91 empirical models.

92 According to this idea, our study proposes an optimized semi-empirical physical
93 model (RF-PMRS) based on the PMRS theory, which attempts to explore the possibility
94 of combining physical models and ML. To be specific, we creatively embed ML (the
95 random forest model) into the PMRS method to simulate the physical parameter (i.e.,

96 VE_f) derived from FMF and related variables, thus optimizing the previous polynomial
 97 expression. Besides, to further improve the $PM_{2.5}$ retrieval accuracy, the physical-deep
 98 learning FMF (Phy-DL FMF) dataset generated by a hybrid retrieval algorithm of ML
 99 and physical mechanisms is introduced. Ultimately, we comprehensively validate the
 100 performance of the $PM_{2.5}$ obtained by our optimized approach.

101 The remained part of our article is as follows. Section 2 describes the experimental
 102 datasets. Section 3 illustrates the specific derivation process of the proposed method.
 103 Section 4 analyzes the evaluation results. Some supporting experiments are discussed
 104 in Section 5. And the final part provides the conclusion.

105

106 **2. Data**

107 **2.1. AERONET data**

108 The Aerosol Robotic Network (AERONET) is a federation of ground-based sun-sky
 109 radiometer networks, providing worldwide remote sensing aerosol data for more than
 110 25 years (Holben et al., 1998). Until now, the Version 3 dataset has been released (Giles
 111 et al., 2017). Due to its high quality, the data from AERONET have been regarded as
 112 theoretical true values to evaluate satellite-based products in related studies (Chen et
 113 al., 2020; Gao et al., 2016; Wang et al., 2019). AOD, FMF, and Volume Size
 114 Distribution products with Level 2.0 (quality-assured) are applied to calculate the true
 115 values of the physical parameters, and then to implement our modeling purpose (not
 116 involved in $PM_{2.5}$ calculations). A total of 9 AERONET sites corresponding to four
 117 typical aerosol types participate in the training. Table 1 shows the specific information.

118

119 **Table 1.** Data information of 9 AERONET sites classified by aerosol types. Location indicates the
 120 latitude and longitude, where ‘-’ means the south latitude and west longitude. Two sites in bold fonts
 121 participate in the $PM_{2.5}$ validation experiment.

Aerosol Type	Site	Location (LAT, LON)	Training period	Isolated- validation period
	Beijing	39.98°, 116.38°	2001-2017	2018-2019
Urban- industrial	Beijing-CAMS	39.93°, 116.32°	2012-2017	2018-2019
	XiangHe	39.75°, 116.96°	2004-2017	/
	Ascension Island	-7.98°, -14.41°	2010-2017	2018-2019

	Capo Verde	16.73°, -22.94°	2010-2017	2018
Biomass burning	CUIABA	-15.73°, -56.07°	2010-2017	2018-2019
	MIRANDA			
Desert dust	GSFC	38.99°, -76.84°	2010-2017	2018-2019
	Mexico City	19.33°, -99.18°	2010-2017	/
Oceanic	Solar Village	24.91°, 46.40°	2010-2013	/

122

123 **2.2. MODIS AOD**

124 MCD19A2, the Moderate-resolution Imaging Spectroradiometer (MODIS) C6
125 Level-2 gridded (L2G) land AOD product (Lyapustin and Wang, 2015), is selected in
126 this study. It is derived from the Multi-Angle Implementation of the Atmospheric
127 Correction (MAIAC) algorithm, which can improve the accuracy in cloud detection
128 and aerosol retrieval (Lyapustin et al., 2011). Besides, this new advanced algorithm
129 jointly combines MODIS Terra and Aqua into a single sensor (Lyapustin et al., 2014).
130 The product is produced daily with a 1km resolution, including aerosol parameters such
131 as 470nm/550nm AOD, quality assurance (QA), and uncertainty factors.

132 The processing of MCD19A2 data (HDF format) is mainly divided into five steps:
133 AOD/QA band extraction, best quality AOD selection, Terra/Aqua data synthesis,
134 missing information reconstruction, and mosaic. Finally, the daily AOD distribution in
135 GeoTiff format is obtained.

136

137 **2.3. Phy-DL FMF dataset**

138 The original global land FMF products have poor data integrity and low accuracy.
139 To enhance their reliability, Yan et al. (2022) have released a satellite-based dataset
140 called Phy-DL FMF, which integrates physical and deep learning methods. Specifically,
141 it selects the FMF data obtained by a physical method (i.e., Look-Up-Table-based
142 Spectral Deconvolution Algorithm, LUT-SDA) as the optimization target (Yan et al.,
143 2017). Then it combines the Phy-based FMF into a deep-learning model along with
144 multiple auxiliary data such as satellite observations for the final Phy-DL results. Note
145 that the process is trained with AERONET data as the ground truth. The product has a
146 spatial resolution of 1° and covers from 2001 to 2020 (daily scale). In the comparison

147 experiment against the ground FMF, Phy-DL FMF shows a higher accuracy ($R = 0.78$,
148 $RMSE = 0.100$) than MODIS FMF ($R = 0.37$, $RMSE = 0.282$) (Yan et al., 2022).

149

150 **2.4. Meteorological data**

151 The meteorological data are obtained from the ERA5 dataset, including the values of
152 planetary boundary layer height (PBLH) and relative humidity (RH). As the fifth-
153 generation reanalysis product released by the European Center for Medium-Range
154 Weather Forecasts (ECMWF), ERA5 provides atmospheric data at 0.25° every hour
155 based on the data assimilation principle (Hersbach et al., 2018). It should be noted that
156 RH is not archived directly in ERA5, thus should be calculated by 2m temperature T
157 and dew point temperature T_d (referred to ERA-Interim: documentation).

$$158 \quad RH = 100 \times \frac{e_s(T_d)}{e_s(T)} \quad (1)$$

159 Here, $e_s(t)$ represents the saturation vapor pressure related to a Celsius temperature
160 t (Simmons et al., 1999).

$$161 \quad e_s(t) = 6.112 \times \exp\left(\frac{17.67 \times t}{t + 243.5}\right) \quad (2)$$

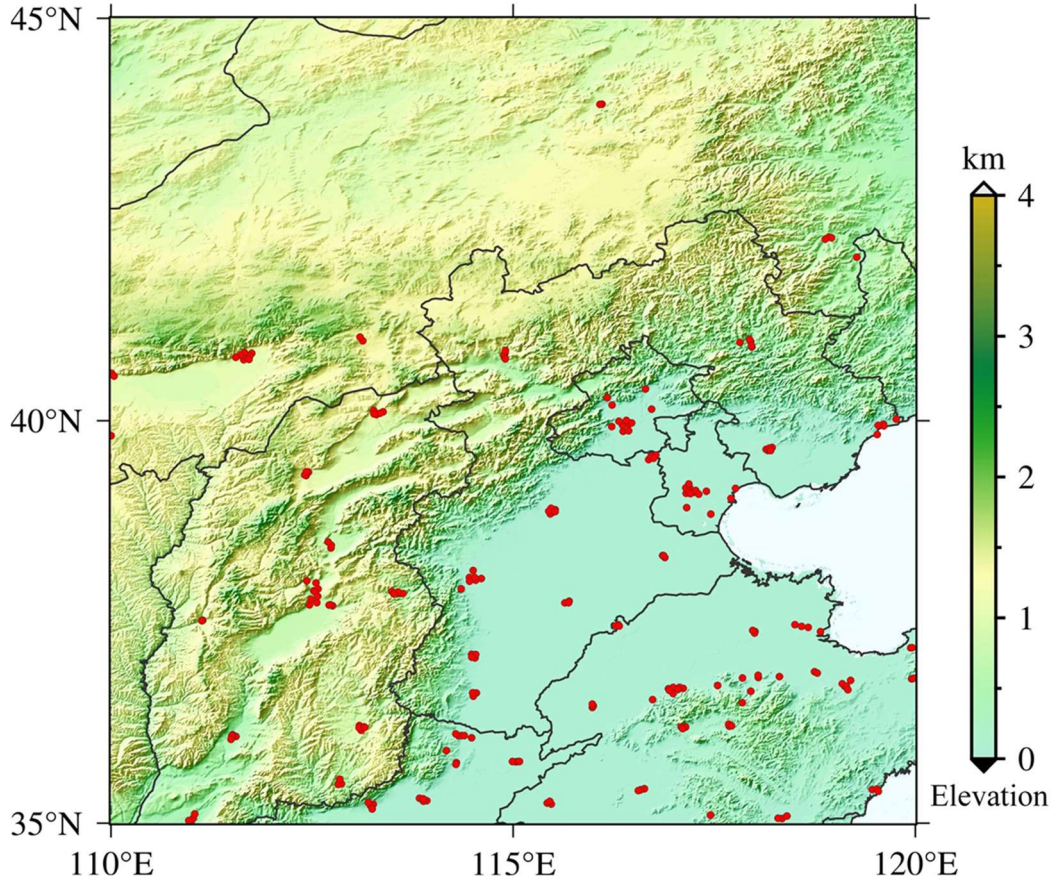
162

163 **2.5. Ground PM_{2.5} measurements**

164 The North China Region (NC) is chosen as the main experimental validation area for
165 the final PM_{2.5} calculations. The near-surface hourly PM_{2.5} values are obtained from the
166 China National Environmental Monitoring Center (CNEMC). Nowadays, over 1600
167 ground-based monitors are working continuously and a total of 232 stations (in 2017)
168 participate in this work. Fig. 1 displays the site distributions of the NC region.

169

The location of PM_{2.5} stations in NC



170 110°E 115°E 120°E
 171 **Fig. 1.** The location of PM_{2.5} ground monitoring stations in the NC region (35°-45°N, 110°-120°E).
 172 The red points represent the PM_{2.5} stations.

173

174 3. Methods

175 Based on the basic physical properties of atmospheric aerosols, the semi-physical
 176 empirical approach starts from the integration of PM mass concentration and AOD.
 177 Then it combines several key factors related to PM_{2.5}, to derive the in situ PM_{2.5}
 178 concentration through multiple remote sensing variables (Koelemeijer et al., 2006). The
 179 overall empirical relationship can be represented as:

$$180 \quad PM_{2.5} = AOD \frac{\rho}{H \cdot f(RH)} S \quad (3)$$

181 where ρ denotes the particle density and H denotes the atmospheric boundary layer
 182 height. $f(RH)$ represents the hygroscopic growth factor related to relative humidity
 183 (RH). S is an optical characteristic parameter that should be simulated.

184

185 3.1. PMRS method

186 3.1.1. The expression of VE_f

187 To illustrate S more precisely, PMRS defines the columnar volume-to-extinction ratio
188 of fine particles (i.e., VE_f), which can be regarded as the basis of our optimization
189 method. So equation (3) is transformed into:

$$190 \quad PM_{2.5} = AOD \frac{\rho}{H \cdot f(RH)} VE_f \quad (4)$$

191 Related to particle size, aerosol extinction, and other properties, VE_f can be expressed
192 as:

$$193 \quad VE_f = \frac{V_{f,column}}{AOD_f} \quad (5)$$

$$194 \quad AOD_f = AOD \cdot FMF \quad (6)$$

195 Here, AOD_f is the fine particle AOD and FMF is the fine mode fraction. $V_{f,column}$
196 can be expressed by the vertical integral of particle volume size distributions (PVSD)
197 within a certain aerodynamic diameter range:

$$198 \quad V_{f,column} = \int_0^{D_{p,c}} V(D_p) dD_p \quad (7)$$

199 $D_{p,c}$ represents the cutting diameter, and the empirical value of $2.0 \mu\text{m}$ is chosen based
200 on previous literature (Hand and Kreidenweis, 2002; Hänel and Thudium, 1977). And
201 $V(D_p)$ represents the PVSD corresponding to the geometric equivalent diameter (D_p).

202

203 3.1.2. Specific process and limitations

204 The PMRS method is developed from equation (4). Based on satellite AOD, the near-
205 surface $PM_{2.5}$ can be obtained through multi-step transformation. Fig. 2(a) shows its
206 specific process. Each arrow refers to a step, respectively: size cutting (output: AOD_f),
207 volume visualization (output: $V_{f,column}$), bottom isolation (output: V_f , fine particle
208 volume near the ground), particle drying (output: $V_{f,dry}$, dry V_f) and $PM_{2.5}$ weighting.
209 The overall expression is as follows:

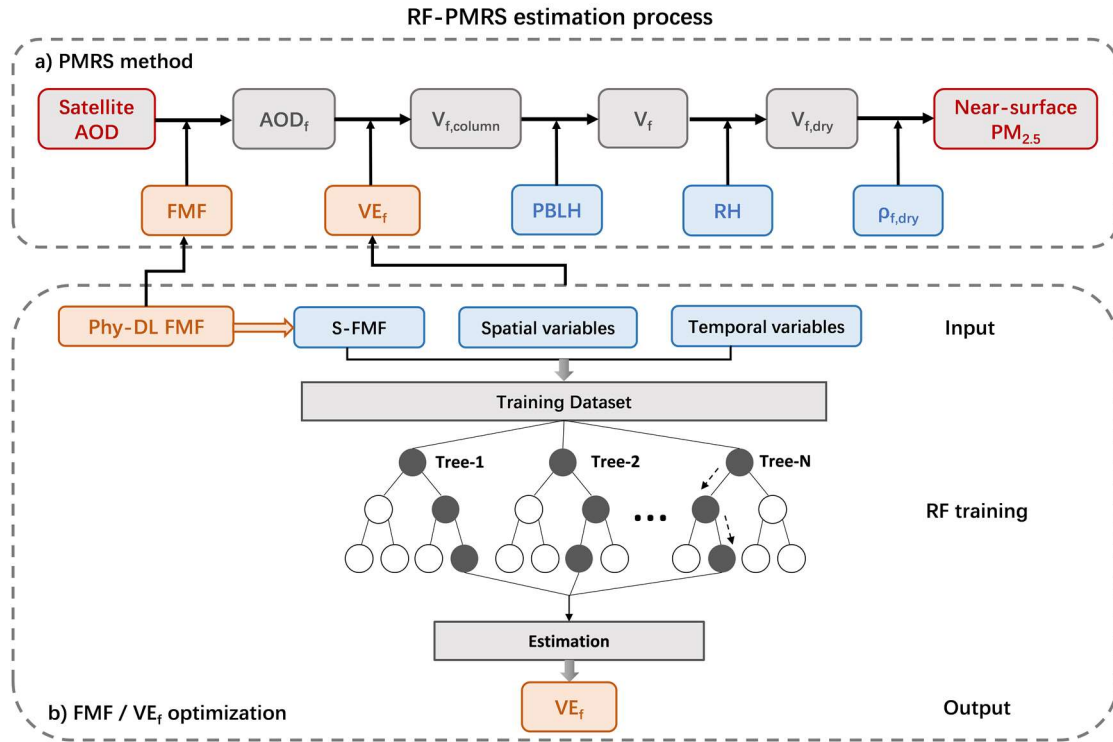
$$210 \quad PM_{2.5} = AOD \frac{FMF \cdot VE_f \cdot \rho_{f,dry}}{PBLH \cdot f_0(RH)} \quad (8)$$

211
$$f_0(RH) = \left(1 - \frac{RH}{100}\right)^{-1} \quad (9)$$

212 where FMF denotes the fine mode fraction, $\rho_{f,dry}$ denotes the dry mass density of
 213 $PM_{2.5}$, and $PBLH$ represents the planet boundary layer height. $f_0(RH)$ represents the
 214 approximation of $f(RH)$ in equation (4), as expressed in equation (9). Considering the
 215 aerosol types in different regions, PMRS fits VE_f to a quadratic polynomial relation of
 216 FMF (Zhang and Li, 2015):

217
$$VE_f = 0.2887FMF^2 - 0.4663FMF + 0.356 \quad (0.1 \leq FMF \leq 1.0) \quad (10)$$

218



219 **Fig. 2.** Surface $PM_{2.5}$ estimation flow of RF-PMRS. a) The five steps of the PMRS method. Gray
 220 boxes are the intermediate outputs, blue boxes are the input data, and orange ones denote the
 221 variables to be optimized. b) The specific optimization of RF-PMRS: FMF dataset replacement and
 222 VE_f simulation by RF model.
 223

224

225 PMRS has strong physical significance, the calculation steps are well-defined and
 226 site-independent. Zhang and Li (2015) tested the performance of PMRS on 15 stations,
 227 and the validation results had an uncertainty of 34%. Compared with the ground value
 228 of Jinhua city in China, a 31.3% relative error was generated in Li et al. (2016). Besides,
 229 Zhang et al. (2020) applied it to the $PM_{2.5}$ change analysis and prediction experiments

230 in China over 20 years. However, there may be a more complex nonlinear relationship
231 between VE_f with FMF, not just a simple quadratic formula. Since VE_f is related to the
232 aerosol type, adding other spatiotemporal variables may optimize the fitting process.
233 Additionally, high-quality FMF data is the basic guarantee for the estimated $PM_{2.5}$
234 quality. In a word, to further improve the physical method, a better nonlinear model
235 between VE_f and related variables from reliable datasets needs to be explored.

236

237 **3.2. Optimization method: RF-PMRS**

238 Therefore, to overcome the above disadvantages, an optimized method called RF-
239 PMRS is proposed. Fig. 2(b) shows the process of our method, while optimizations for
240 FMF and VE_f are described separately below.

241 **1) FMF dataset selection**

242 We introduce the Phy-DL FMF dataset into the PMRS method to improve the
243 accuracy of size-cutting results. In terms of performance, it exhibits higher accuracy
244 and wider space-time coverage than satellite products (Yan, 2021). See the data section
245 for details.

246

247 **2) VE_f simulation based on ML**

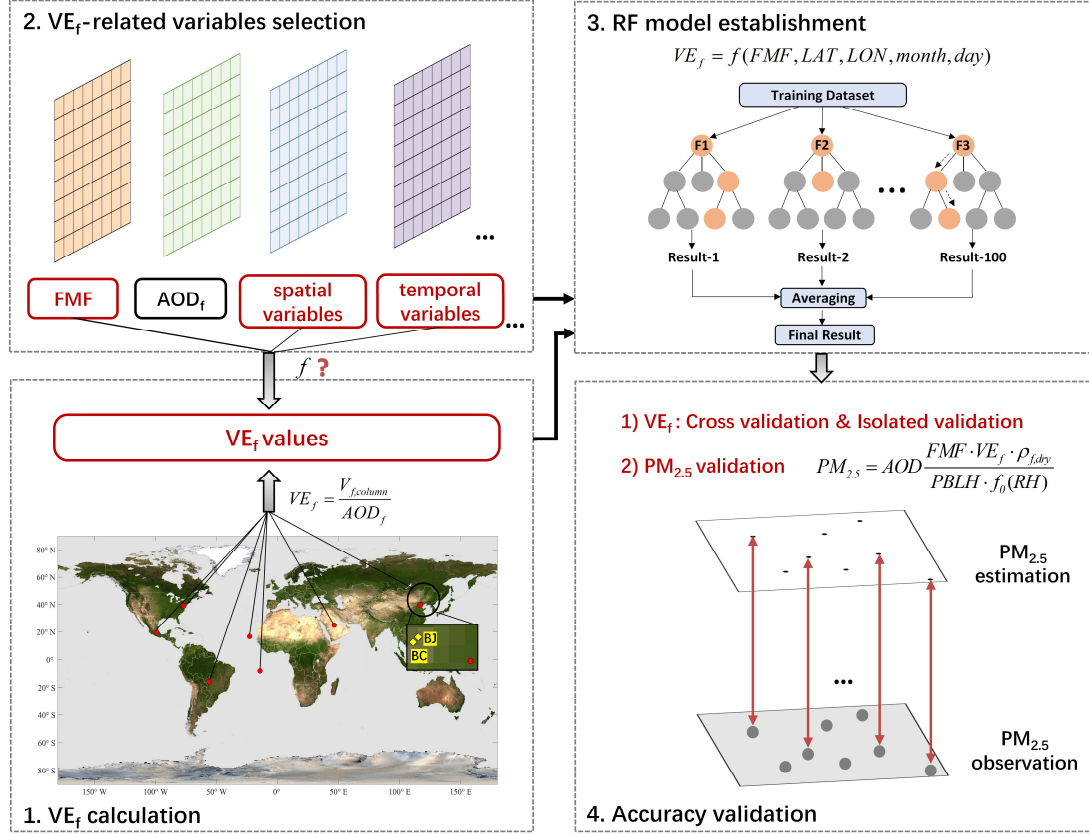
248 The main idea is to establish an ML model between the VE_f truth obtained from
249 multiple AERONET sites and related variables, thus improving the subsequent VE_f -
250 simulation accuracy (Fig. 3).

251

252 **Step 1 VE_f calculation**

253 The VE_f true values are calculated concerning equations (5)-(7). Due to the
254 spatiotemporal variability of different aerosol types, we calculate the VE_f values at 9
255 AERONET stations around the world (Table 1) to train a universal model. The first step
256 in Fig. 3 shows their distribution characteristics. Among them, Beijing and Beijing-
257 CAMS sites are highlighted since they participate in the subsequent point validation
258 experiment.

259



260

261 **Fig. 3.** Specific steps for simulating VE_f based on ML in our RF-PMRS method. The map used in
 262 step 1 is from NASA Visible Earth ([https://visibleearth.nasa.gov/images/57752/blue-marble-land-](https://visibleearth.nasa.gov/images/57752/blue-marble-land-surface-shallow-water-and-shaded-topography)
 263 [surface-shallow-water-and-shaded-topography](https://visibleearth.nasa.gov/images/57752/blue-marble-land-surface-shallow-water-and-shaded-topography)). The red points in step 1 represent the distribution
 264 of the 9 AERONET sites and the two yellow quadrangles in the zoom-in view highlight the Beijing
 265 (BJ) and Beijing-CAMS (BC) sites.

266 Step 2 VE_f -related variables selection

267 According to the theory, FMF is selected as the most important modeling variable.
 268 Previous studies have also shown that the FMF- VE_f relationship has a good single-
 269 value correspondence, which is not affected by AOD. Compared with AOD_f and
 270 $V_{f,column}$, FMF is a better indicator for estimation (Zhang and Li, 2015). In addition,
 271 considering the spatiotemporal heterogeneity of VE_f , the latitude, longitude (LAT,
 272 LON), and data time (month, day) of each site are added to the training.

273

274 Step 3 RF model establishment

275 From step 2, VE_f can be expressed as:

$$276 \quad VE_f = f(FMF, LAT, LON, month, day) \quad (11)$$

277 We optimize VE_f expression based on random forest (RF). RF is made up of multiple
278 decision trees that can build high-accuracy models based on fewer variables (Svetnik
279 et al., 2003; Yang et al., 2020). This ensemble ML method randomly samples the
280 training dataset to form multiple subsets and random combinations of features are
281 selected in node splitting (Belgiu and Drăguț, 2016). The specific process is to 1)
282 generate training subsets, 2) build an optimal model, and 3) calculate the result (Fig. 3
283 shows its flowchart). Note that the station FMF values (S-FMF) from AERONET sites
284 are used when training.

285

286 **Step 4 Accuracy validation**

287 The VE_f estimation is also based on equation (11), where f is the optimal relationship
288 after RF parameter adjustment, and Phy-DL FMF is applied to realize the extension of
289 model results from point to surface. 10-fold cross-validation (CV) (Rodriguez et al.,
290 2009) and isolated-validation (IV) are used to evaluate model performance (For details
291 of the validation methods, see Appendix A1).

292

293 **3) $PM_{2.5}$ value estimation and evaluation**

294 Then, calculate $PM_{2.5}$ according to the corresponding process (equation (8)). The
295 variables (in sections 2.2 to 2.4) are spatially matched to ground sites at their respective
296 resolutions. And based on UTC, the $PM_{2.5}$ validation is conducted on a daily scale in
297 2017. Because of the effective quantity of the AERONET public dataset and MODIS
298 data, we choose 2017 as the representative year. Note that we select the measured
299 empirical value of $\rho_{f,dry}$ (i.e., 1.5 g/cm^3) for the NC region from Gao et al. (2007).

300 The statistical indicators used in the evaluation include correlation coefficient (R),
301 mean bias (MB), relative mean bias (RMB), root mean square error (RMSE), and mean
302 absolute error (MAE). In addition, relative predictive error (RPE) is added to validate
303 the accuracy of the RF-based VE_f model. See Appendix A2 for the specific information
304 on these indicators.

305

306 **4. Experiment results**

307 Three main experiments are conducted to verify the proposed RF-PMRS method,
 308 and the specific information is shown in Table 2.

309 **Table 2.** A brief information summary of the experiments conducted in our study.

Experiment	Object	Region	Period	Time scale
Model performance for training VE_f	VE_f	Global scale (Nine AERONET sites)	CV: Training period in Table 1 IV: Isolated-validation period in Table 1 (See Appendix A1)	Daily
Accuracy evaluation of PMRS/RF-PMRS	$PM_{2.5}$	Two AERONET Sites: Beijing, Beijing-CAMS	2017	Daily
Generalization performance of RF-PMRS	$PM_{2.5}$	North China region	2017	Daily

310

311 **4.1. RF model performance for training VE_f**

312 The simulation model of VE_f is trained based on the data in Table 1. Specifically, the
 313 10-fold CV result is used to determine the optimal combination of parameters for the
 314 model, and see Appendix A3 for the adjustment of the model parameters. Considering
 315 that the completeness of the training data will optimize the generalization performance
 316 of the model, the experiment fine-tunes the model based on all the original datasets (the
 317 training period of Table 1) under the optimal parameters, then the final RF model is
 318 constructed. This is also the most common method for ML model construction. Next,
 319 the IV experiment provides independent time validation of the final model.

320 Table 3 shows the CV and IV results to respectively demonstrate the internal and
 321 external accuracy of the final RF model. It can be seen that RF can capture the complex
 322 relationship between VE_f and related variables well. R is as high as 0.974 (0.975),
 323 RMSE and MAE are both small, and RPE is around 30%, which suggests the desired
 324 estimation accuracy. Overall, the CV results represent the great performance of the RF
 325 model for extracting information, that is, the relationship of multi-source data to VE_f .
 326 In the meantime, the statistical results in CV and IV experiments are similar, indicating
 327 that the RF model has no obvious overfitting phenomenon.

328

329 **Table 3.** Performance statistics of the RF model for training VE_f . N represents the number of data,
330 and VE_f has no unit.

	R	RMSE	RPE	MAE	N
Cross-validation (CV)	0.974	0.076	32.9%	0.034	6463
Isolated-validation (IV)	0.975	0.067	29.8%	0.037	814

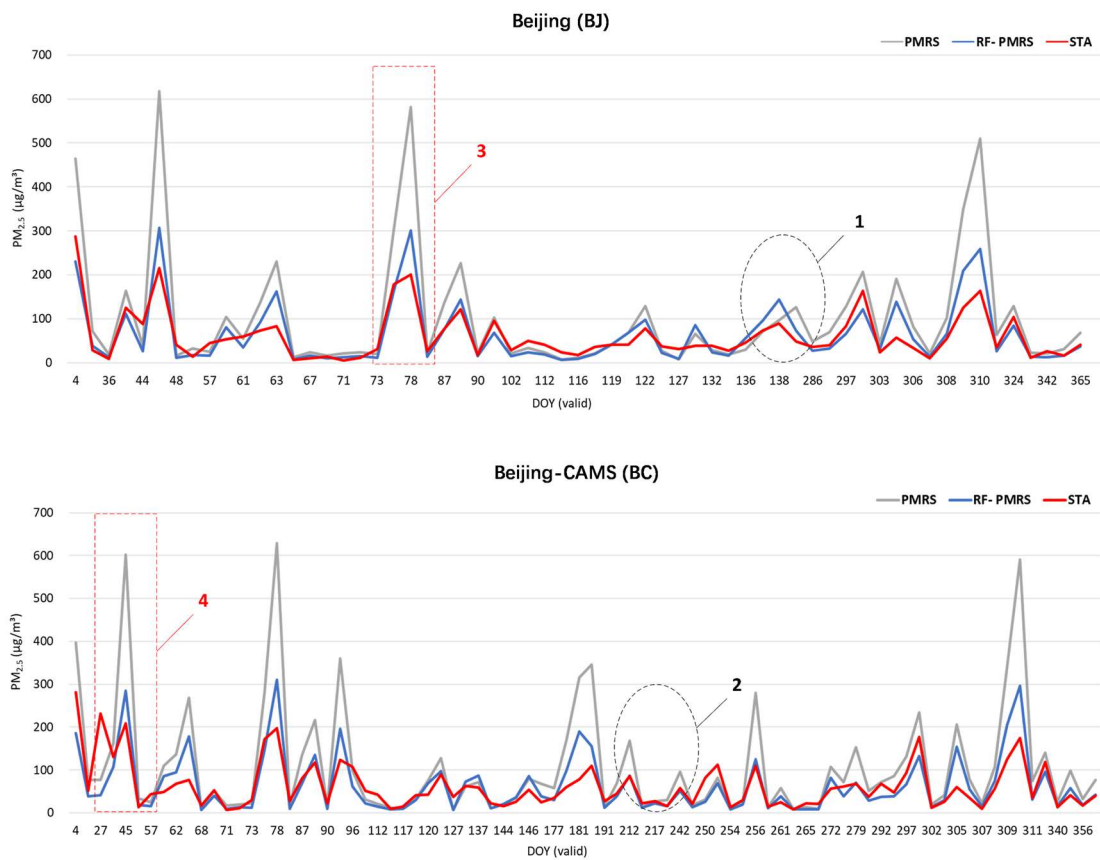
331

332 **4.2. Accuracy evaluation of PMRS/RF-PMRS at AERONET stations**

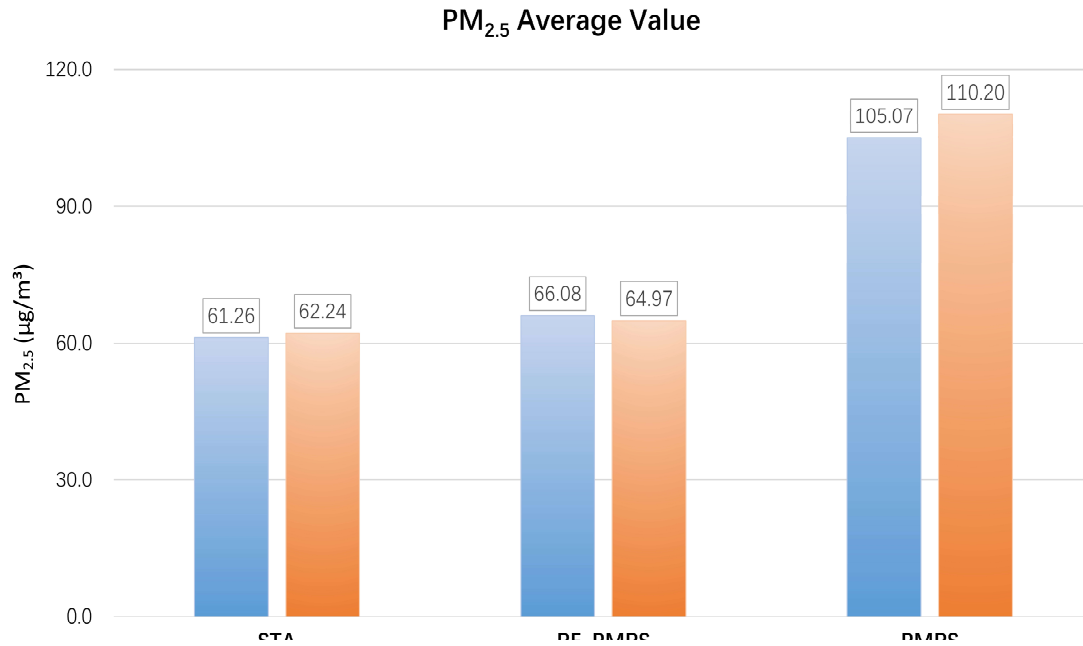
333 The purpose of RF-PMRS is to construct an optimal model from the obtained point
334 matching data pairs, and generalize it to the space-time continuous surface data for VE_f
335 derivation. In the subsequent experiments in sections 4.2 and 4.3, the VE_f values are
336 obtained by introducing the Phy-DL FMF dataset (surface data) to the final RF model.
337 At the same time, the Phy-DL FMF data is also applied to the $PM_{2.5}$ calculation process
338 (FMF variable in Equation 8) for a wide range of $PM_{2.5}$ concentration.

339 Then, the experiment compares $PM_{2.5}$ results of PMRS and RF-PMRS at Beijing (BJ)
340 and Beijing-CAMS (BC) AERONET sites in 2017. Here, RF-PMRS simulates VE_f
341 based on RF, replacing the polynomial of the PMRS method. Note that the results of
342 the two sites are compared with their respective nearest ground $PM_{2.5}$ stations (distances
343 of 3.64 km and 3.91 km, respectively, in line with the representative range of ground
344 stations in previous studies (Shi et al., 2018)). Fig. 4 displays the time series of $PM_{2.5}$
345 values for different models at two sites. The blue line fits the red line better than the
346 gray one, confirming that the $PM_{2.5}$ results of RF-PMRS are closer to the true values.
347 Within the range of the black circles at positions 1 and 2, the variation of RF-PMRS
348 results has better consistency with the ground truth, while the PMRS results show
349 dislocation and excessive growth. The overall performance of the RF-PMRS
350 estimations can signify the effectiveness of our proposed method framework. As
351 observed in the red boxes at positions 3 and 4, both models have a certain degree of
352 deviation, which is found to be consistent with the time regularity of the AOD high
353 values. Meanwhile, Fig. B1 (in Appendix B) plots the bias time series between
354 PMRS/RF-PMRS and in-situ values. As can be seen, the bias of the optimization
355 method (RF-PMRS) is stably distributed around zero, which greatly reduces the
356 numerical uncertainty. And it is worth noting that our method has well mitigated the

357 apparent overestimation of the original model (PMRS) in the case of above-normal
 358 aerosol loadings. Furthermore, the average $PM_{2.5}$ values from ground stations, PMRS,
 359 and RF-PMRS are compared. As for the two sites, the RF-PMRS results are satisfactory.
 360 As depicted in Fig. 5, the RF-PMRS and station mean values are close, with a difference
 361 of $4.82 \mu\text{g}/\text{m}^3$ (BJ) and $2.73 \mu\text{g}/\text{m}^3$ (BC), suggesting a good estimation. Nevertheless,
 362 the PMRS results have deviations greater than $40 \mu\text{g}/\text{m}^3$, and overestimation exists at
 363 both sites. It can be inferred that, in our proposed method, the optimization of VE_f can
 364 greatly improve the $PM_{2.5}$ estimation accuracy.



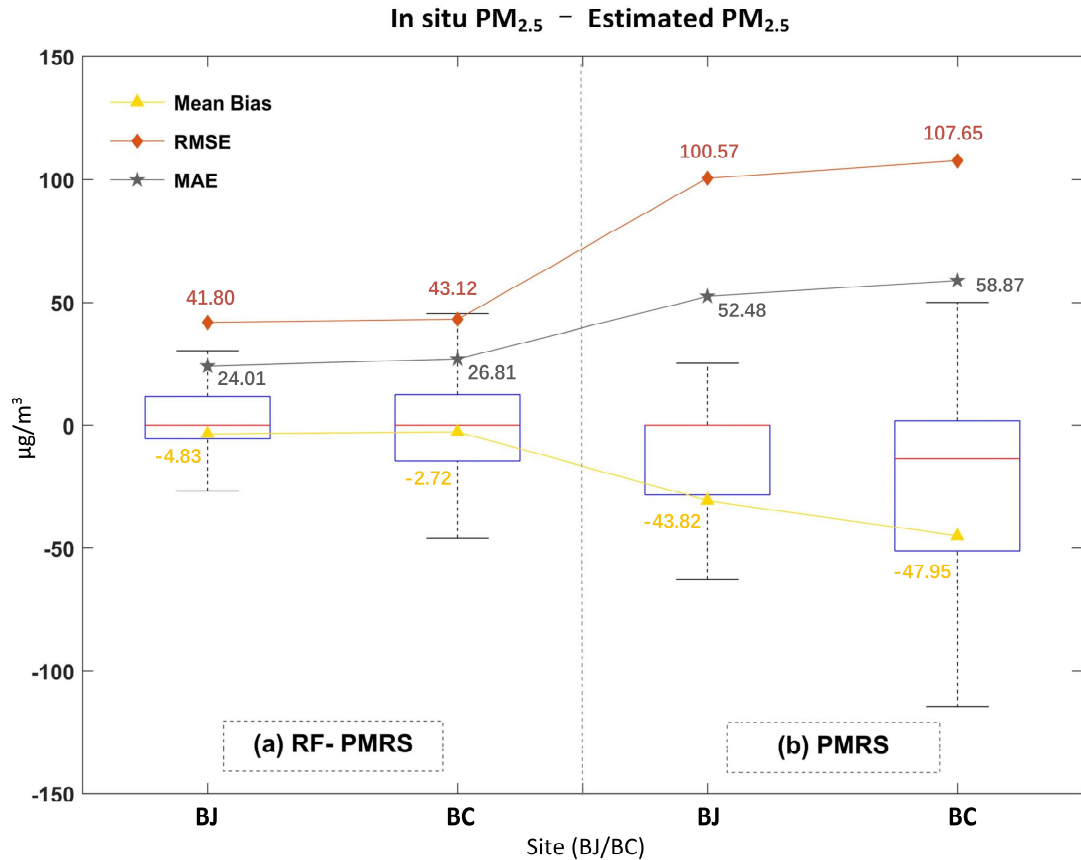
365
 366 **Fig. 4.** Three $PM_{2.5}$ time series at the Beijing (BJ) and Beijing-CAMS (BC) sites under their
 367 respective DOYs in 2017. Here, DOY (valid) means the day of the year with valid AOD, FMF, and
 368 other $PM_{2.5}$ -related data. Grey, blue, and red lines represent $PM_{2.5}$ values of PMRS, RF-PMRS, and
 369 stations (STA), respectively. The red boxes and black circles select a specific period for analysis.
 370



371
 372 **Fig. 5.** Annual average PM_{2.5} values from stations (left), RF-PMRS (middle), and PMRS model
 373 (right) at the BJ and BC sites.

374 Aiming at visually comparing the optimization effect, Fig. 6 plots the PM_{2.5} bias
 375 distribution patterns for two methods. From the boxplot, the average PM_{2.5} bias of RF-
 376 PMRS is close to zero (less than 5 µg/m³), which is greatly lower than that of PMRS.
 377 Besides, PMRS PM_{2.5} has a larger deviation range, which manifests in two aspects. One
 378 is the maximum bias, specifically, it has exceeded 100 µg/m³ at the BC site. The other
 379 is the overall distribution of the data bias, the BJ site ones are mostly distributed below
 380 zero, indicating an obvious overestimation. As for RF-PMRS, the above circumstances
 381 are not obviously reflected in it. In addition, as can be seen from the indicators, RMSE
 382 and MAE of RF-PMRS PM_{2.5} decrease by about half in comparison with PMRS. And
 383 the experiment has confirmed that the RF-PMRS PM_{2.5} values have a strong linear
 384 relationship with the ground truth at both sites, with R around 0.8 (0.82 at BJ and 0.78
 385 at BC). Such a large optimization effect is attributed to the VE_f expression replacement
 386 to the fitted RF model.

387



388

389 **Fig. 6.** Boxplots of RF-PMRS (a) and PMRS (b) PM_{2.5} bias at the BJ and BC sites. The upper (lower)
 390 black line of each box represents the largest (smallest) value, the blue upper (lower) border
 391 represents the upper (lower) quartile, and the red line denotes the median. Besides, the yellow,
 392 orange, and gray symbols are the MB, RMSE, and MAE of the corresponding PM_{2.5} concentration.

393

394 4.3. Generalization performance of RF-PMRS

395 Then, we estimate PM_{2.5} based on PMRS and RF-PMRS within North China in 2017
 396 (Fig. 1 exhibits the distribution pattern of the validation stations). Table 4 shows the
 397 accuracy statistics. It can be seen that RF-PMRS greatly reduces the bias (about
 398 44.87%), with MB of about 2.31 $\mu\text{g}/\text{m}^3$. Similar to the results at the sites, the RF-PMRS
 399 method can derive PM_{2.5} concentration with practically no overestimation
 400 (underestimation). Although there is not much difference in R values of the two models
 401 (R of RF-PMRS is only improved by 0.01), RMSE and MAE of which decrease by
 402 about 39.96 $\mu\text{g}/\text{m}^3$ and 18.86 $\mu\text{g}/\text{m}^3$, respectively. As a result, the optimized method
 403 deserves to be considered excellent.

404

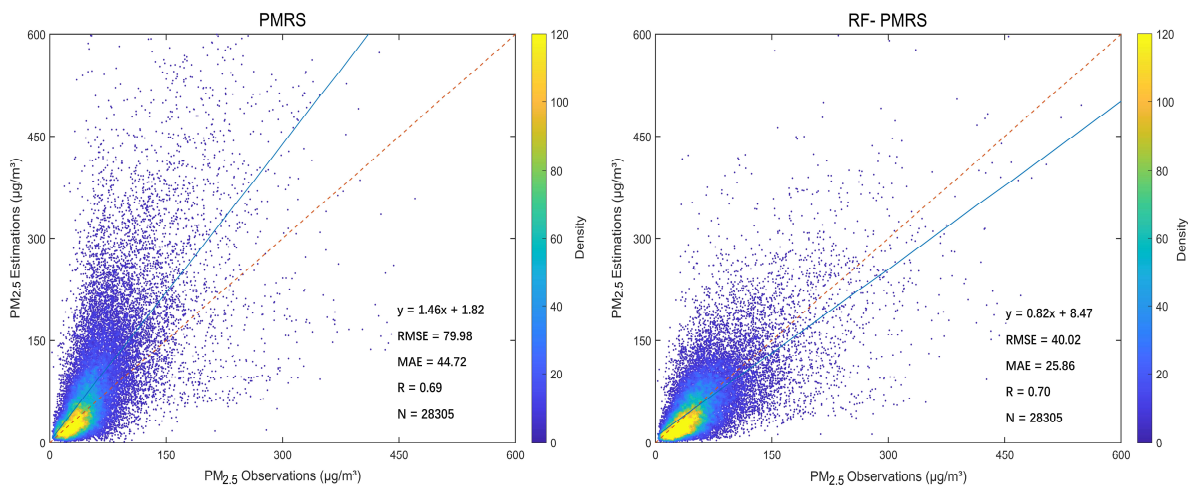
405 **Table 4.** Validation results of PMRS and RF-PMRS PM_{2.5} in North China.

Method	R	MB ($\mu\text{g}/\text{m}^3$)	RMB (%)	RMSE ($\mu\text{g}/\text{m}^3$)	MAE ($\mu\text{g}/\text{m}^3$)
PMRS	0.69	-29.34	48.71%	79.98	44.72
RF-PMRS	0.70	2.31	3.84%	40.02	25.86

406

407 Meanwhile, PM_{2.5} scatterplots are presented below. As depicted in Fig. 7, there are
 408 sufficient estimated samples (28305) in the NC region, which guarantees the credibility
 409 of our validation results. In general, the RF-PMRS PM_{2.5} values are distributed around
 410 the 1:1 reference line evenly, with a slightly higher R of 0.70 compared to that of the
 411 original method. And the slope of the linear fitting relationship reaches 0.82, which
 412 indicates that the proposed method greatly reduces the overestimation of PMRS with a
 413 linear slope of 1.46. Although the overall performance of the RF-PMRS estimations
 414 maintains an excellent level, defects do remain. To be specific, in areas with high PM_{2.5}
 415 concentration (especially greater than 150 $\mu\text{g}/\text{m}^3$), RF-PMRS results exist a slight
 416 underestimation. It may be caused by the relatively small number of high-value PM_{2.5}
 417 points (only 1319 out of 28305), which is difficult to adequately reflect the fitting effect
 418 of the method.

419



420

421 **Fig. 7.** Validation scatterplots of PM_{2.5} results from PMRS (left) and RF-PMRS (right). Red dashed
 422 lines are 1:1 reference lines, and blue solid lines stand for the linear fits. The right legends show the
 423 point densities (frequency) represented by different colors.

424

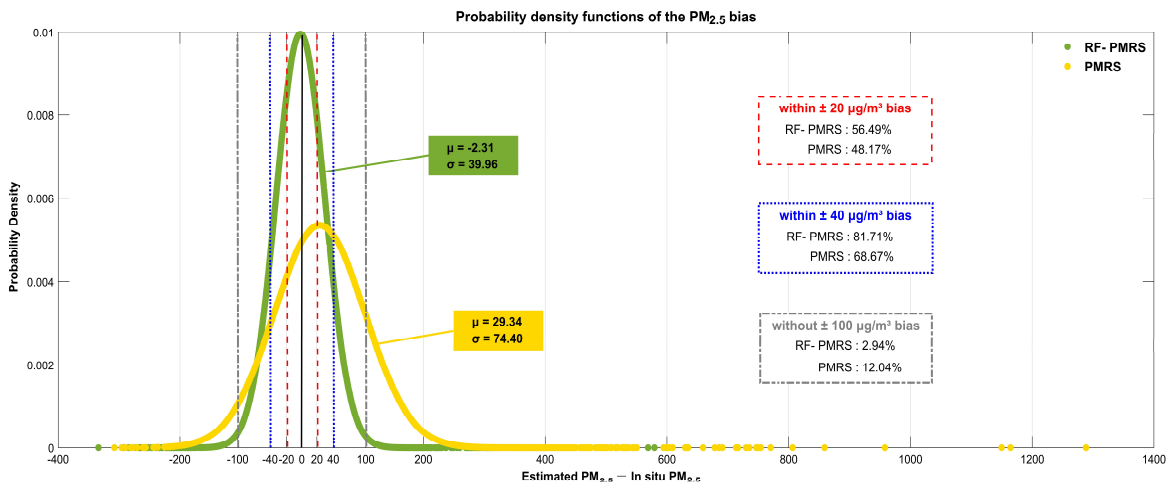
425 As for RF-PMRS, the deviation is reduced to a large extent, so the probability density

426 function maps based on the bias of PMRS and RF-PMRS are further drawn. Fig. 8
 427 visualizes the probability densities within different bias ranges. In terms of distribution
 428 characteristics, the overall bias of RF-PMRS from the zero value (black solid line) is
 429 small. About the curve shape, it is high and narrow, manifesting that the bias has a lower
 430 standard deviation (STD) and is more prone to appear around the mean. However,
 431 PRMS shows a more discrete distribution pattern, and there are many outliers outside
 432 the range of greater than $600 \mu\text{g}/\text{m}^3$. Simultaneously, as can be concluded from the three
 433 boxes, within the bias range of $\pm 20 \mu\text{g}/\text{m}^3$ and $\pm 40 \mu\text{g}/\text{m}^3$, the data numbers of RF-
 434 PMRS results increase by 8.32% and 12.81%, respectively. Outside the range of ± 100
 435 $\mu\text{g}/\text{m}^3$, the number decreases by 9.10%. Therefore, as far as the accuracy is concerned,
 436 RF-PMRS results have lower bias and better stability.

437

438 In addition to the above general performance comparison in Section 4.3, Fig. 9
 439 presents the annual average RMSE spatial distribution of PMRS and RF-PMRS $\text{PM}_{2.5}$
 440 at NC stations. The two methods show a large deviation in the middle and southeast,
 441 and the RMSE map of PMRS has more red points. However, RF-PMRS can weaken
 442 this phenomenon very well since its RMSE representative colors are generally light. In
 443 particular, the proportion of dark red sites (RMSE greater than $60 \mu\text{g}/\text{m}^3$) decreases
 444 from 65.44% (PMRS) to 4.15% (RF-PMRS). In the areas where the ground stations are
 445 clustered, the deviation also reduces significantly.

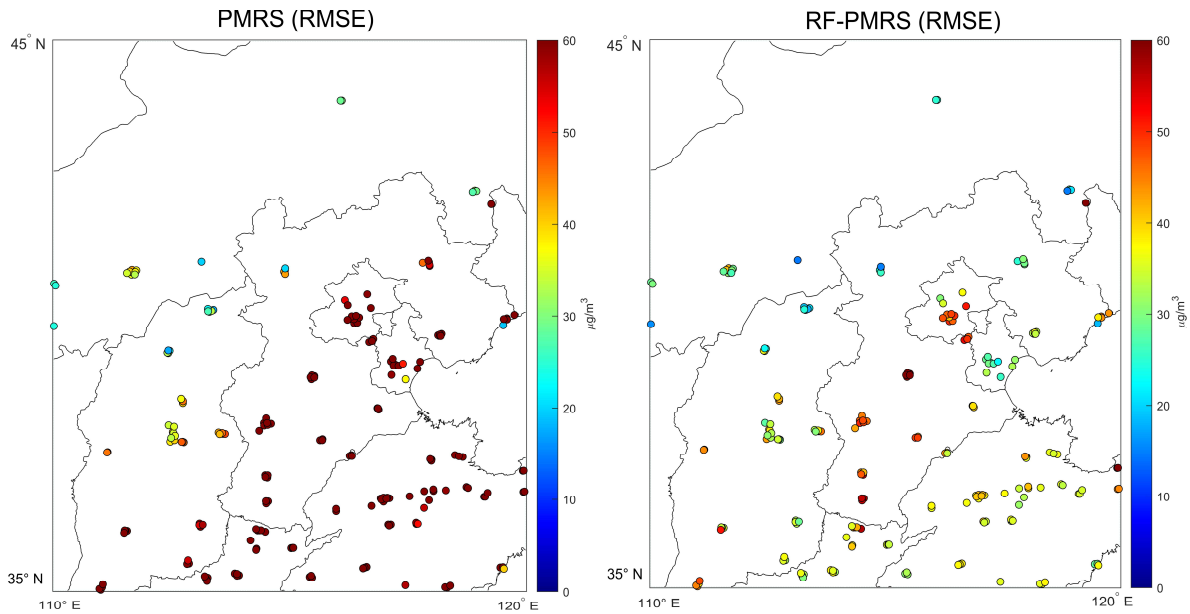
446



447

448 **Fig. 8.** Probability density functions of PMRS (yellow) and RF-PMRS (green) $\text{PM}_{2.5}$ bias. The red,

449 blue and grey dotted lines indicate the bias boundaries of $\pm 20 \mu\text{g}/\text{m}^3$, $\pm 40 \mu\text{g}/\text{m}^3$, and $\pm 100 \mu\text{g}/\text{m}^3$,
 450 respectively. μ and σ represent the mean value and standard deviation of each data.
 451



452 **Fig. 9.** RMSE of the year-average $\text{PM}_{2.5}$ concentration values between different models and ground
 453 stations (left: PMRS $\text{PM}_{2.5}$, right: RF-PMRS $\text{PM}_{2.5}$). Note that the top red of the RMSE legend
 454 indicates RMSE values equal to or greater than $60 \mu\text{g}/\text{m}^3$.
 455

456

457 In a word, the above analysis demonstrates that compared with the simple quadratic
 458 polynomial relationship (equation (10)), the established RF model in RF-PMRS can
 459 more accurately capture the relationship between VE_f and multiple variables, thereby
 460 improving the $\text{PM}_{2.5}$ estimation accuracy.

461

462 5. Discussion

463 5.1. Accuracy comparison of PMRS using MODIS/Phy-DL FMF

464 To confirm the superiority of the Phy-DL FMF data adopted in our method
 465 framework, taking the BJ and BC sites as examples (in 2017), the experiment compares
 466 the $\text{PM}_{2.5}$ accuracy and the number of effective days calculated by PMRS based on
 467 different FMF. Table 5 presents the overall day-level results. Here, ‘DOY’ means the
 468 day of the year and ‘valid’ means that all variables related to the $\text{PM}_{2.5}$ calculation are
 469 valid. As can be seen, after the FMF replacement, the valid DOY turns out to become
 470 more (an increase of 113 days), which illustrates that the number of effective $\text{PM}_{2.5}$

471 concentrations has gone up by about 5 times. Moreover, the accuracy has been
 472 significantly enhanced, with R increased by about 0.30, RMSE and MAE decreased by
 473 26.14% and 16.47% accordingly. On the whole, Phy-DL FMF contributes to the
 474 improvement of PMRS results, signifying the first step optimization of the proposed
 475 RF-PMRS method is effective.

476

477 **Table 5.** Validation results of the PMRS method using different FMF data. The valid DOY refers to
 478 the number of days that the AOD, FMF, and other data are not missing when calculating $PM_{2.5}$. Note
 479 that since the valid days of the two schemes are different, the MB and RMB are not compared.

	Valid DOY	R	RMSE ($\mu\text{g}/\text{m}^3$)	MAE ($\mu\text{g}/\text{m}^3$)
PMRS with MODIS FMF	30	0.38	63.01	35.64
PMRS with Phy-DL FMF	143	0.68	46.54	29.77

480

481 5.2. Performance compared with other ML models

482 Different machine learning models are suitable for diverse research data, and
 483 decision tree (DT) models can better fit experiments with fewer variables, such as this
 484 study. For comparison, except for RF, the Extremely Randomized Tree (ERT) (Geurts
 485 et al., 2006) and Gradient Boosting Decision Tree (GBDT) (Friedman, 2001) models
 486 have also been established. The results of training VE_f based on the above three DT
 487 models are presented in Table 6 and Table 7. By contrast, RF performs best in CV and
 488 IV experiments, as indicated by the multiple accuracy indicators. Although ERT and
 489 GBDT models are comparable to RF in some indicators, there exists a certain degree
 490 of overfitting in the above two models, which is manifested in that their IV results are
 491 clearly worse than their respective CV ones. Thus, the RF model is applied to our study.

492

493 **Table 6.** Cross-validation results in comparison of the decision tree models for training VE_f . N
 494 represents the number of data, and VE_f has no unit.

CV results					
	R	RMSE	RPE	MAE	N
RF	0.974	0.076	0.330	0.034	6463
ERT	0.972	0.079	0.343	0.035	
GBDT	0.973	0.078	0.339	0.036	

495

496 **Table 7.** Isolated-validation results in comparison of the decision tree models for training VE_f . The
 497 indicators are the same as those in Table 6.

IV results					
	R	RMSE	RPE	MAE	N
RF	0.975	0.067	0.299	0.037	814
ERT	0.967	0.076	0.340	0.042	
GBDT	0.969	0.074	0.331	0.040	

498

499 5.3. Feature importance of the embedded RF model

500 Additionally, the feature importance of RF is calculated to evaluate the contribution
 501 of model predictors to VE_f simulation. Fig. B2 (in Appendix B) shows the results by
 502 normalization (taking 100 as the total). Without a doubt, FMF accounts for the largest
 503 proportion, about 76.4%, which is consistent with the analysis when selecting the VE_f -
 504 related variables (see Section 3.2). The contribution of spatiotemporal variables is about
 505 1/3 of FMF, which indirectly affirms the credibility of RF feature learning. Also, it
 506 provides a basis for further uncertainty optimization of VE_f and $PM_{2.5}$ accuracy.

507

508 5.4. Advantages and disadvantages

509 5.4.1. Advantages of the RF-PMRS method

510 From the perspective of model parameter optimization, this paper embeds RF to
 511 replace the subprocess parameter of the semi-empirical physical model. As a result, the
 512 proposed method, RF-PMRS, reduces the uncertainty of the complex physical
 513 parameter (i.e., VE_f) based on the estimation steps of strong physical significance, and
 514 realizes the coupling of machine learning and model mechanism. The proposed method
 515 does not rely on the $PM_{2.5}$ values of ground stations and is not affected by the station
 516 density and distribution mode, which can estimate the $PM_{2.5}$ concentration
 517 independently.

518 Meanwhile, as for the method, we construct the VE_f model based on RF using high-
 519 precision point data and extend it to surface data for $PM_{2.5}$ estimations. The
 520 experimental results demonstrate the overall performance of the model (Section 4.1)
 521 and its applicability in North China (Sections 4.2 to 4.3), showing that the method has

522 certain universality from point scale to surface scale.

523 1) The overall performance of the model is high. We use the ground data of 9
524 AERONET sites around the world to train the RF model and simulate the VE_f values,
525 the site distribution is relatively uniform and the amount of training data is sufficient.
526 Table 1 shows a total of 6463 data matching pairs in the training period, which is enough
527 to establish a credible RF model. Table 3 results show that in IV experiments, the
528 accuracy of the model is well and can be generalized in different periods. For VE_f , the
529 model shows both high internal accuracy (CV) and external accuracy (IV), so it can be
530 generalized in regions with different aerosol types.

531 2) In the subsequent $PM_{2.5}$ estimation, the model displays high applicability in North
532 China. Analyzing the model construction, the four aerosol types are the classification
533 basis of the training data, and comprehensive modeling can improve the generalization
534 performance. Also, the addition of spatiotemporal variables can increase the model
535 applicability in North China. On the other hand, the number of stations used in an area
536 does not determine the regional accuracy of the established model, which can be
537 derived from our results. Compared with the $PM_{2.5}$ ground measurements in the NC
538 region, the relative deviation of the RF-PMRS $PM_{2.5}$ is only $2.31 \mu\text{g}/\text{m}^3$, which confirms
539 that RF can represent the relationships within North China.

540

541 **5.4.2. Limitations on the scope of validation region**

542 However, there are still some shortcomings, mainly manifested in the scope of the
543 validation region. Due to limited experimental data, we only conduct experiments in
544 North China (the main aerosol type is urban-industrial). The main reasons are: 1)
545 insufficient $\rho_{f,dry}$ value. As the empirical value in the semi-physical empirical model,
546 the $\rho_{f,dry}$ value is often obtained by field measurement and induction. The insufficient
547 $\rho_{f,dry}$ values hinder the derivation of $PM_{2.5}$ in other regions and more research results
548 are needed; 2) disclosure limits on global $PM_{2.5}$ ground measurements. Accurate and
549 sufficient in-situ $PM_{2.5}$ values are the basic guarantee for the verification of estimated
550 $PM_{2.5}$ results; 3) fewer public AERONET sites. Therefore, only BJ and BC sites in
551 North China are used for representative point-scale validation.

552

553 **5.4.3. Data differences and uncertainty analysis**

554 In the RF-PMRS method, the VE_f model constructed by high-precision site data is
555 generalized to surface data for validation, and the data types involved are as follows.

556 1) AERONET AOD vs. MODIS AOD

557 Two types of AOD are used for different experimental steps, among which
558 AERONET AOD is applied to calculate the true values of VE_f for establishing the RF
559 simulation model. And the RF model construction is a step of $PM_{2.5}$ estimation (as VE_f
560 variable in equation (8)). MODIS AOD is satellite AOD data, which is the most
561 commonly used remote sensing data for large-scale retrieval of $PM_{2.5}$. It is an important
562 variable for $PM_{2.5}$ estimation in RF-PMRS (as AOD variable in equation (8)). Thus,
563 there is no error in the $PM_{2.5}$ calculation caused by AOD category replacement.

564 As for uncertainty, AERONET AOD provides truth values for calculating VE_f ,
565 which theoretically has negligible uncertainty, and the simulation accuracy of VE_f
566 represents its influence on estimating $PM_{2.5}$ to a certain extent. And it is generally
567 considered that MODIS AOD has guaranteed quality and sufficient accuracy to be used
568 directly.

569 2) S-FMF vs. Phy-DL FMF

570 S-FMF is obtained directly from the AERONET monitoring sites and is one of the
571 variables of the RF model (as FMF variable in equation (11)). In the point-to-surface
572 extension, Phy-DL FMF is introduced into the RF model to replace S-FMF, and the
573 2017 VE_f values are obtained. The basis of the above replacement is that the accuracy
574 of Phy-DL FMF is relatively consistent with that of S-FMF. Besides, Phy-DL FMF data
575 is applied to the $PM_{2.5}$ estimation steps (as FMF variable in equation (8)) for a wider
576 range of validation experiments. The results show that the $PM_{2.5}$ concentration
577 estimated by RF-PMRS has high accuracy, proving the credibility of Phy-DL FMF.

578 3) FMF uncertainty

579 Different surface data sources may affect the $PM_{2.5}$ results, introducing some
580 uncertainty. Section 5.1 compares the $PM_{2.5}$ accuracy using two FMF data in 2017. The
581 data missing time for MODIS FMF and Phy-DL FMF in North China are different,

582 which can be found in the statistics on their respective available days (refer to valid
583 DOY). There are far more valid days based on Phy-DL FMF than MODIS FMF (143
584 and 31 days), demonstrating the superiority of Phy-DL FMF. Although the specific
585 validation time of two FMF varies, the overall accuracy of the PM_{2.5} estimation (which
586 can be regarded as the average accuracy over the year) shows that the Phy-DL FMF
587 increases R to 0.68 (MODIS FMF: 0.38) with low uncertainty.

588 4) $\rho_{f,dry}$ uncertainty

589 As introduced earlier, the $\rho_{f,dry}$ value is often obtained by field measurement. In our
590 study, we select 1.5 g/cm³ as the $\rho_{f,dry}$ value for North China. There are certain variations
591 in the empirical values of different regions, and there will be errors (uncertainty)
592 between the values in Beijing and other places in the NC region. However, our
593 experimental area is not large, and we use 1.5 g/cm³ to represent $\rho_{f,dry}$ of the whole
594 region, which has been applied in previous articles (Zhang and Li, 2015; Li et al., 2016).

595 5) Uncertainty between variable resolutions

596 In most experiments, the lowest resolution of all data will be taken as the unified
597 resolution when obtaining data values. The different data may lose some spatial details
598 during the upsampling/downsampling process, which brings uncertainty to the
599 estimation results. In RF-PMRS method, there is no such uncertainty problem. We set
600 1° as the unified spatial unit, and take the longitude and latitude of each cell's center as
601 the reference longitude and latitude. The variables in the data section are spatially
602 matched to ground sites at their respective resolutions and the space-time matching
603 method has been described in the method section. So, all kinds of data uncertainties
604 only exist in their instrument measurement or statistical release.

605 Overall, RF-PMRS shows excellent estimation performance in North China, and the
606 accuracy of surface PM_{2.5} estimation based on remote sensing data is guaranteed. Next,
607 with the improvement of related experimental data, we will verify our proposed method
608 in a broader range and continuously optimize it from all aspects.

609

610 **6. Conclusion**

611 Among various satellite remote sensing methods for PM_{2.5} retrieval, the semi-

612 empirical physical approach has strong physical significance and clear calculation steps
613 and derives the PM_{2.5} mass concentration independently of in situ observations.
614 However, the parameters with the meaning of optical properties are difficult to express,
615 which need to be optimized. Hence, the study proposes a method (RF-PMRS) that
616 embeds machine learning in a physical model to obtain surface PM_{2.5}: 1) Based on the
617 PMRS method and select the Phy-DL FMF product with a combined mechanism; 2)
618 Use the RF model to fit the parameter VE_f, rather than a simple quadratic polynomial.
619 In the point-to-surface validation, RF-PMRS shows great optimized performance.
620 Experiments at two AERONET sites show that R reaches up to 0.8. And in North China,
621 RMSE decreases by 39.95 µg/m³ with a 44.87% reduction in relative deviation. In the
622 future, we will further explore the combination of atmospheric mechanism and machine
623 learning, then research the PM_{2.5} retrieval methods with physical meaning and higher
624 accuracy.

625

626 **Appendix A: Supplementary description**

627 **A1. 10-fold cross-validation and isolated-validation**

628 The sample-based 10-fold cross-validation method is applied to tune the model
629 parameters and test the internal accuracy of our model. The original dataset is randomly
630 divided into ten parts, nine of which are used as the training set for model fitting, and
631 the remaining one is used for prediction, then the cross-validation process is repeated
632 ten rounds until each data has been used as the test set.

633 At the same time, when verifying the RF-based VE_f model, the dataset in the period
634 that did not participate in the training in Table 1 is used for isolated-validation.

635

636 **A2. Statistical indicators**

$$637 \quad R = \frac{\sum_{i=1}^m (y_i - \bar{y}) \sum_{i=1}^m (f_i - \bar{f})}{\sqrt{\sum_{i=1}^m (y_i - \bar{y})^2} \sqrt{\sum_{i=1}^m (f_i - \bar{f})^2}}$$

$$638 \quad MB = \bar{y} - \bar{f}$$

639
$$RMB = \text{abs}\left(\frac{\bar{y} - \bar{f}}{\bar{y}}\right)$$

640
$$RMSE = \sqrt{\frac{1}{m} \sum_{i=1}^m (y_i - f_i)^2}$$

641
$$MAE = \frac{1}{m} \sum_{i=1}^m |y_i - f_i|$$

642
$$RPE = \frac{\sqrt{\frac{1}{m} \sum_{i=1}^m (y_i - f_i)^2}}{\bar{y}}$$

643 where m is the total number of observations, i is the number of measurements, y_i is the
644 i -th observation, f_i is the corresponding estimation result. And \bar{y} and \bar{f} are the
645 averages of all observations and estimates, respectively.

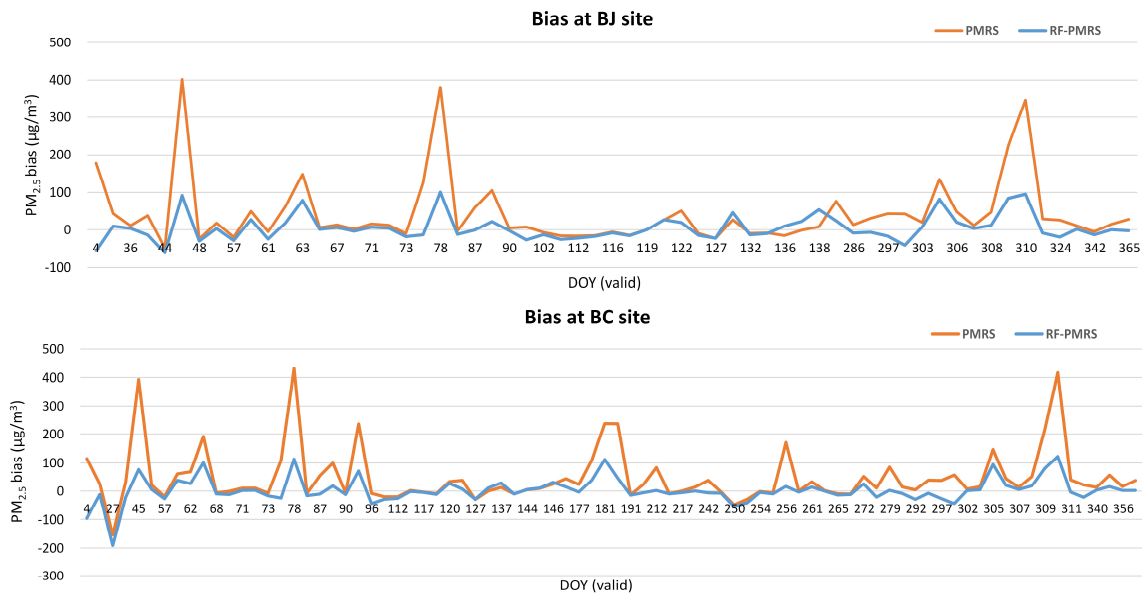
646

647 **A3. Parameter adjustments of the RF model**

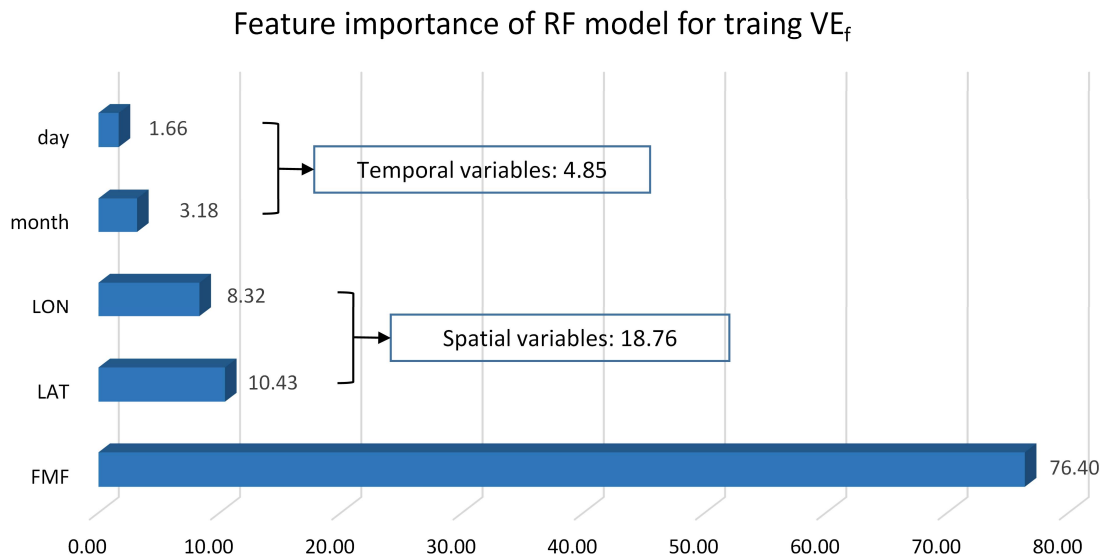
648 The four parameters of RF are adjusted, that is the correlation coefficient r changes
649 with (a) the number of trees, (b) maximum depth, (c) maximum number of features
650 when splitting, (d) minimum number of split samples. Experiments show that the
651 maximum depth varies greatly in a small range. To prevent overfitting, the four
652 parameters of RF are adjusted to 60, 10, 2, and 8. It can ensure high accuracy while
653 improving training efficiency.

654

655 **Appendix B: Figures**



656
 657 **Fig. B1.** The time series of PMRS/RF-PMRS PM_{2.5} bias at the Beijing and Beijing-CAMS sites
 658 under their respective DOYs in 2017. The orange line represents the bias between the PM_{2.5} values
 659 of PMRS and stations, while the blue one indicates the PM_{2.5} difference between RF-PMRS and
 660 stations.
 661



662
 663 **Fig. B2.** The predictor importance results (normalized) of the RF model for training VE_f.
 664

665 **Code and data availability**

666 All relevant codes as well as the intermediate data of this work are archived at
 667 <https://doi.org/10.5281/zenodo.7183822> (Jin, 2022). The MCD19A2 data can be

668 downloaded on <https://ladsweb.modaps.eosdis.nasa.gov> (last access: 30-09-2022)
669 (Lyapustin and Wang, 2015). Detailed information about the Phy-DL FMF dataset can
670 be found at <https://doi.org/10.5281/zenodo.5105617> (Yan, 2021). Meteorological data
671 used in this work are obtained at
672 <https://cds.climate.copernicus.eu/cdsapp#!/dataset/reanalysis-era5-single-levels> (last
673 access: 30-09-2022) (Hersbach et al., 2018). AERONET data was downloaded from
674 <https://aeronet.gsfc.nasa.gov/> (last access: 30-09-2022) (Giles et al., 2019).

675

676 **Author contributions**

677 **Caiyi Jin:** Data curation, Methodology, Formal analysis, Writing - original draft.
678 **Qiangqiang Yuan:** Conceptualization, Supervision, Project administration, Writing -
679 review and editing. **Tongwen Li:** Resources, Methodology, Writing - review and
680 editing, Formal analysis. **Yuan Wang:** Methodology, Validation, Writing - review and
681 editing. **Liangpei Zhang:** Supervision, Writing - review and editing.

682

683 **Competing interests**

684 The contact author has declared that none of the authors has any competing interests.

685

686 **Acknowledgments**

687 We gratefully acknowledge the Atmosphere Archive and Distribution System
688 (LAADS), the ECMWF, the AERONET project, and the CNEMC for respectively
689 providing the MODIS products, the meteorological data, the ground aerosol data, and
690 the surface PM_{2.5} concentration. We also thank other institutions which provide related
691 data in this work.

692

693 **Financial support**

694 This research was funded in part by the National Natural Science Foundation of
695 China (No. 41922008 and No. 42201359), the Hubei Science Foundation for
696 Distinguished Young Scholars (No. 2020CFA051) and the Guangdong Basic and
697 Applied Basic Research Foundation (No. 2022A1515010492).

698

699 **References**

700 Belgiu, M., and Drăguț, L.: Random forest in remote sensing: A review of applications
701 and future directions, *ISPRS J. Photogramm. Remote Sens.*, 114, 24-31,
702 <https://doi.org/10.1016/j.isprsjprs.2016.01.011>, 2016.

703 Bowe, B., Xie, Y., Li, T., Yan, Y., Xian, H., and Al-Aly, Z.: The 2016 global and
704 national burden of diabetes mellitus attributable to PM2.5 air pollution, *Lancet Planet.
705 Health*, 2, e301-e312, [https://doi.org/10.1016/S2542-5196\(18\)30140-2](https://doi.org/10.1016/S2542-5196(18)30140-2), 2018.

706 Chen, X., de Leeuw, G., Arola, A., Liu, S., Liu, Y., Li, Z., and Zhang, K.: Joint retrieval
707 of the aerosol fine mode fraction and optical depth using MODIS spectral reflectance
708 over northern and eastern China: Artificial neural network method, *Remote Sens
709 Environ*, 249, 112006, <https://doi.org/10.1016/j.rse.2020.112006>, 2020.

710 Friedman, J.H.: Greedy function approximation: a gradient boosting machine, *Ann Stat*,
711 29(5), 1189–1232, <http://www.jstor.org/stable/2699986>, 2001.

712 Gao, J., Zhou, Y., Wang, J., Wang, T., and Wang, W.X.: Inter-comparison of WPSTM-
713 TEOMTM-MOUDITM and investigation on particle density, *Huan Jing Ke Xue*, 28,
714 1929-1934, <https://doi.org/10.3321/j.issn:0250-3301.2007.09.005>, 2007.

715 Gao, L., Li, J., Chen, L., Zhang, L., and Heidinger, A.K.: Retrieval and validation of
716 atmospheric aerosol optical depth from AVHRR over China, *IEEE Trans Geosci
717 Remote Sens*, 54, 6280-6291, <https://doi.org/10.1109/TGRS.2016.2574756>, 2016.

718 Geng, G., Zhang, Q., Martin, R.V., van Donkelaar, A., Huo, H., Che, H., Lin, J., and
719 He, K.: Estimating long-term PM2.5 concentrations in China using satellite-based
720 aerosol optical depth and a chemical transport model, *Remote Sens Environ*, 166, 262-
721 270, <https://doi.org/10.1016/j.rse.2015.05.016>, 2015.

722 Geurts, P., Ernst, D., and Wehenkel, L.: Extremely randomized trees, *Mach Learn*, 63,
723 3-42, <https://doi.org/10.1007/s10994-006-6226-1>, 2006.

724 Giles, D.M., Holben, B.N., Eck, T.F., Smirnov, A., Sinyuk, A., Schafer, J., Sorokin,
725 M.G., and Slutsker, I.: Aerosol robotic network (AERONET) version 3 aerosol optical
726 depth and inversion products, in: American Geophysical Union (AGU) 98th Fall
727 Meeting Abstracts, New Orleans, America, 11-15 December 2017, A11O-01, 2017.

728 Giles, D. M., Sinyuk, A., Sorokin, M. G., Schafer, J. S., Smirnov, A., Slutsker, I., Eck,
729 T. F., Holben, B. N., Lewis, J. R., Campbell, J. R., Welton, E. J., Korkin, S. V., and
730 Lyapustin, A. I.: Advancements in the Aerosol Robotic Network (AERONET) Version
731 3 database - automated near-real-time quality control algorithm with improved cloud
732 screening for Sun photometer aerosol optical depth (AOD) measurements, *Atmos Meas*
733 *Tech*, 12, 169–209, <https://doi.org/10.5194/amt-12-169-2019>, 2019.

734 Gupta, P., and Christopher, S.A.: Particulate matter air quality assessment using
735 integrated surface, satellite, and meteorological products: Multiple regression approach,
736 *J. Geophys. Res. Atmos.*, 114, D14205, <https://doi.org/10.1029/2008JD011496>, 2009.

737 Hand, J.L., and Kreidenweis, S.M.: A new method for retrieving particle refractive
738 index and effective density from aerosol size distribution data, *Aerosol Sci Technol*, 36,
739 1012-1026, <https://doi.org/10.1080/02786820290092276>, 2002.

740 Hänel, G., and Thudium, J.: Mean bulk densities of samples of dry atmospheric aerosol
741 particles: A summary of measured data, *Pure Appl. Geophys.*, 115, 799-803,
742 <https://doi.org/10.1007/BF00881211>, 1977.

743 He, J., Yuan, Q., Li, J., and Zhang, L.: PoNet: A universal physical optimization-based
744 spectral super-resolution network for arbitrary multispectral images, *Inform Fusion*, 80,
745 205-225, <https://doi.org/10.1016/j.inffus.2021.10.016>, 2022.

746 He, J., Li, J., Yuan, Q., Shen, H., and Zhang, L.: Spectral Response Function-Guided
747 Deep Optimization-Driven Network for Spectral Super-Resolution, *IEEE Trans Neural*
748 *Netw. Learn. Syst.*, PP(99), 1-15, <https://doi.org/10.1109/TNNLS.2021.3056181>, 2021.

749 Hersbach, H., Bell, B., Berrisford, P., Biavati, G., Horányi, A., Muñoz Sabater, J.,
750 Nicolas, J., Peubey, C., Radu, R., Rozum, I., Schepers, D., Simmons, A., Soci, C., Dee,
751 D., Thépaut, J.-N.: ERA5 hourly data on single levels from 1979 to present, Copernicus
752 Climate Change Service (C3S) Climate Data Store (CDS) [data set], (Accessed on 30-
753 09-2022), <https://doi.org/10.24381/cds.adbb2d47>, 2018.

754 Holben, B.N., Eck, T.F., Slutsker, I., Tanré, D., Buis, J.P., Setzer, A., Vermote, E.,
755 Reagan, J.A., Kaufman, Y.J., Nakajima, T., Lavenu, F., Jankowiak, I., and Smirnov, A.:
756 AERONET — A federated instrument network and data archive for aerosol

757 characterization, *Remote Sens Environ*, 66, 1-16, <https://doi.org/10.1016/S0034->
758 [4257\(98\)00031-5](https://doi.org/10.1016/S0034-4257(98)00031-5), 1998.

759 Irrgang, C., Boers, N., Sonnewald, M., Barnes, E.A., Kadow, C., Staneva, J., and
760 Saynisch-Wagner, J.: Towards neural Earth system modelling by integrating artificial
761 intelligence in Earth system science, *Nat. Mach. Intell.*, 3, 667-674,
762 <https://doi.org/10.1038/s42256-021-00374-3>, 2021.

763 Jin, C.: An optimized semi-empirical physical approach for satellite-based PM2.5
764 retrieval: using random forest model to simulate the complex parameter, Zenodo [code],
765 <https://doi.org/10.5281/zenodo.7183822>, 2022.

766 Koelemeijer, R.B.A., Homan, C.D., and Matthijsen, J.: Comparison of spatial and
767 temporal variations of aerosol optical thickness and particulate matter over Europe,
768 *Atmospheric Environ.*, 40, 5304-5315, <https://doi.org/10.1016/j.atmosenv.2006.04.044>,
769 2006.

770 Kokhanovsky, A.A., Prikhach, A.S., Katsev, I.L., and Zege, E.P.: Determination of
771 particulate matter vertical columns using satellite observations, *Atmos Meas Tech*, 2,
772 327-335, <https://doi.org/10.5194/amt-2-327-2009>, 2009.

773 Lee, J.-B., Lee, J.-B., Koo, Y.-S., Kwon, H.-Y., Choi, M.-H., Park, H.-J., and Lee, D.-
774 G.: Development of a deep neural network for predicting 6 h average PM2.5
775 concentrations up to 2 subsequent days using various training data, *Geosci. Model Dev.*,
776 15, 3797–3813, <https://doi.org/10.5194/gmd-15-3797-2022>, 2022.

777 Li, T., Shen, H., Zeng, C., Yuan, Q., and Zhang, L.: Point-surface fusion of station
778 measurements and satellite observations for mapping PM2.5 distribution in China:
779 Methods and assessment, *Atmospheric Environ.*, 152, 477-489,
780 <https://doi.org/10.1016/j.atmosenv.2017.01.004>, 2017.

781 Li, Z., Zhang, Y., Shao, J., Li, B., Hong, J., Liu, D., Li, D., Wei, P., Li, W., Li, L.,
782 Zhang, F., Guo, J., Deng, Q., Wang, B., Cui, C., Zhang, W., Wang, Z., Lv, Y., Xu, H.,
783 Chen, X., Li, L., and Qie, L.: Remote sensing of atmospheric particulate mass of dry
784 PM2.5 near the ground: Method validation using ground-based measurements, *Remote*
785 *Sens Environ*, 173, 59-68, <https://doi.org/10.1016/j.rse.2015.11.019>, 2016.

786 Lyapustin, A., Wang, Y., Laszlo, I., Kahn, R., Korkin, S., Remer, L., Levy, R., and

787 Reid, J.S.: Multiangle implementation of atmospheric correction (MAIAC): 2. Aerosol
788 algorithm, *J. Geophys. Res. Atmos.*, 116, D03211,
789 <https://doi.org/10.1029/2010JD014986>, 2011.

790 Lyapustin, A., Wang, Y., Xiong, X., Meister, G., Platnick, S., Levy, R., Franz, B.,
791 Korkin, S., Hilker, T., Tucker, J., Hall, F., Sellers, P., Wu, A., and Angal, A.: Scientific
792 impact of MODIS C5 calibration degradation and C6+ improvements, *Atmos Meas*
793 *Tech*, 7, 4353-4365, <https://doi.org/10.5194/amt-7-4353-2014>, 2014.

794 Lyapustin, A., and Wang, Y.: MCD19A2 MODIS/Terra+Aqua Aerosol Optical
795 Thickness Daily L2G Global 1km SIN Grid, NASA LP DAAC [data set], (Accessed
796 on 30-09-2022), <http://doi.org/10.5067/MODIS/MCD19A2.006>, 2015.

797 Lyu, B., Huang, R., Wang, X., Wang, W., and Hu, Y.: Deep-learning spatial principles
798 from deterministic chemical transport models for chemical reanalysis: an application in
799 China for PM_{2.5}, *Geosci. Model Dev.*, 15, 1583–1594, [https://doi.org/10.5194/gmd-](https://doi.org/10.5194/gmd-15-1583-2022)
800 [15-1583-2022](https://doi.org/10.5194/gmd-15-1583-2022), 2022.

801 Ma, Z., Hu, X., Huang, L., Bi, J., and Liu, Y.: Estimating ground-Level PM_{2.5} in China
802 using satellite remote sensing, *Environ. Sci. Technol.*, 48, 7436-7444,
803 <https://doi.org/10.1021/es5009399>, 2014.

804 Pope III, C.A., Burnett, R.T., Thun, M.J., Calle, E.E., Krewski, D., Ito, K., and Thurston,
805 G.D.: Lung cancer, cardiopulmonary mortality, and long-term exposure to fine
806 particulate air pollution, *JAMA*, 287, 1132-1141,
807 <https://doi.org/10.1001/jama.287.9.1132>, 2002.

808 Raut, J., and Chazette, P.: Assessment of vertically-resolved PM₁₀ from mobile lidar
809 observations, *Atmospheric Chem. Phys.*, 9, 8617-8638, [https://doi.org/10.5194/acp-9-](https://doi.org/10.5194/acp-9-8617-2009)
810 [8617-2009](https://doi.org/10.5194/acp-9-8617-2009), 2009.

811 Rodriguez, J.D., Perez, A., and Lozano, J.A.: Sensitivity analysis of k-fold cross
812 validation in prediction error estimation, *IEEE Trans. Pattern Anal. Mach. Intell.*, 32,
813 569-575, <https://doi.org/10.1109/TPAMI.2009.187>, 2009.

814 Shi, X., Zhao, C., Jiang, J.H., Wang, C., Yang, X., and Yung, Y.L.: Spatial
815 representativeness of PM_{2.5} concentrations obtained using observations from network
816 stations, *J. Geophys. Res. Atmos.*, 123, 3145-3158,

817 <https://doi.org/10.1002/2017JD027913>, 2018.

818 Simmons, A.J., Untch, A., Jakob, C., Källberg, P., and Undén, P.: Stratospheric water
819 vapour and tropical tropopause temperatures in ECMWF analyses and multi-year
820 simulations, *Q J R Meteorol Soc*, 125, 353-386,
821 <https://doi.org/10.1002/qj.49712555318>, 1999.

822 Svetnik, V., Liaw, A., Tong, C., Culberson J.C., Sheridan R.P., and Feuston, B.P.:
823 Random Forest: A Classification and Regression Tool for Compound Classification
824 and QSAR Modeling, *J. Chem. Inf. Comput. Sci.*, 43, 6, 1947-1958,
825 <https://doi.org/10.1021/ci034160g>, 2003.

826 Van Donkelaar, A., Martin, R.V., and Park, R.J.: Estimating ground-level PM_{2.5} using
827 aerosol optical depth determined from satellite remote sensing, *J. Geophys. Res. Atmos.*,
828 111, D21201, <https://doi.org/10.1029/2005JD006996>, 2006.

829 Wang, Y., Yuan, Q., Li, T., Shen, H., Zheng, L., and Zhang, L.: Evaluation and
830 comparison of MODIS Collection 6.1 aerosol optical depth against AERONET over
831 regions in China with multifarious underlying surfaces, *Atmospheric Environ.*, 200,
832 280-301, <https://doi.org/10.1016/j.atmosenv.2018.12.023>, 2019.

833 Wu, X., Wang, Y., He, S., and Wu, Z.: PM_{2.5}/PM₁₀ ratio prediction based on a long
834 short-term memory neural network in Wuhan, China, *Geosci. Model Dev.*, 13, 1499–
835 1511, <https://doi.org/10.5194/gmd-13-1499-2020>, 2020.

836 Xiao, Y., Wang, Y., Yuan, Q., He, J., and Zhang, L.: Generating a long-term
837 (2003–2020) hourly 0.25° global PM_{2.5} dataset via spatiotemporal downscaling of
838 CAMS with deep learning (DeepCAMS), *Sci. Total Environ.*, 848, 157747,
839 <https://doi.org/10.1016/j.scitotenv.2022.157747>, 2022.

840 Xu, P., Chen, Y., and Ye, X.: Haze, air pollution, and health in China, *Lancet*, 382,
841 2067, [https://doi.org/10.1016/S0140-6736\(13\)62693-8](https://doi.org/10.1016/S0140-6736(13)62693-8), 2013.

842 Yan, X., Zang, Z., Li, Z., Luo, N., Zuo, C., Jiang, Y., Li, D., Guo, Y., Zhao, W., Shi,
843 W., and Cribb, M.: A global land aerosol fine-mode fraction dataset (2001--2020)
844 retrieved from MODIS using hybrid physical and deep learning approaches, *Earth Syst.*
845 *Sci. Data*, 14, 1193-1213, <https://doi.org/10.5194/essd-14-1193-2022>, 2022.

846 Yan, X., Li, Z., Shi, W., Luo, N., Wu, T., and Zhao, W.: An improved algorithm for

847 retrieving the fine-mode fraction of aerosol optical thickness, part 1: Algorithm
848 development, *Remote Sensing of Environment*, 192, 87-97,
849 <https://doi.org/10.1016/j.rse.2017.02.005>, 2017.

850 Yan, X.: Physical and deep learning retrieved fine mode fraction (Phy-DL FMF),
851 Zenodo [data set], (Accessed on 30-09-2022), <https://doi.org/10.5281/zenodo.5105617>,
852 2021.

853 Yang, Q., Yuan, Q., Li, T., and Yue, L.: Mapping PM2.5 concentration at high
854 resolution using a cascade random forest based downscaling model: Evaluation and
855 application, *J. Clean. Prod.*, 277, 123887,
856 <https://doi.org/10.1016/j.jclepro.2020.123887>, 2020.

857 Yuan, Q., Shen, H., Li, T., Li, Z., Li, S., Jiang, Y., Xu, H., Tan, W., Yang, Q., Wang,
858 J., Gao, J., and Zhang, L.: Deep learning in environmental remote sensing:
859 Achievements and challenges, *Remote Sens Environ*, 241, 111716,
860 <https://doi.org/10.1016/j.rse.2020.111716>, 2020.

861 Zhang, Y., Li, Z., Bai, K., Wei, Y., Xie, Y., Zhang, Y., Ou, Y., Cohen, J., Zhang, Y.,
862 Peng, Z., Zhang, X., Chen, C., Hong, J., Xu, H., Guang, J., Lv, Y., Li, K., and Li, D.:
863 Satellite remote sensing of atmospheric particulate matter mass concentration:
864 Advances, challenges, and perspectives, *Fundamental Research*, 1, 240-258,
865 <https://doi.org/10.1016/j.fmre.2021.04.007>, 2021.

866 Zhang, Y., Li, Z., Chang, W., Zhang, Y., de Leeuw, G., and Schauer, J.J.: Satellite
867 observations of PM2.5 changes and driving factors based forecasting over China 2000–
868 2025, *Remote Sens.*, 12(16), 2518, <https://doi.org/10.3390/rs12162518>, 2020.

869 Zhang, Y., and Li, Z.: Remote sensing of atmospheric fine particulate matter (PM2.5)
870 mass concentration near the ground from satellite observation, *Remote Sens Environ*,
871 160, 252-262, <https://doi.org/10.1016/j.rse.2015.02.005>, 2015.